

SC-VAE: Sparse Coding-based Variational Autoencoder with Learned ISTA

Pan Xiao Peijie Qiu Sungmin Ha Abdalla Bani Shuang Zhou Aristeidis Sotiras

Washington University School of Medicine, Washington University in St. Louis

{panxiao, peijie.qiu, sungminha, a.bani, shuangzhou, aristeidis.sotiras}@wustl.edu

Abstract

Learning rich data representations from unlabeled data is a key challenge towards applying deep learning algorithms in downstream tasks. Several variants of variational autoencoders (VAEs) have been proposed to learn compact data representations by encoding high-dimensional data in a lower dimensional space. Two main classes of VAEs methods may be distinguished depending on the characteristics of the meta-priors that are enforced in the representation learning step. The first class of methods derives a continuous encoding by assuming a static prior distribution in the latent space. The second class of methods learns instead a discrete latent representation using vector quantization (VQ) along with a codebook. However, both classes of methods suffer from certain challenges, which may lead to suboptimal image reconstruction results. The first class suffers from posterior collapse, whereas the second class suffers from codebook collapse. To address these challenges, we introduce a new VAE variant, termed sparse coding-based VAE with learned ISTA (SC-VAE), which integrates sparse coding within variational autoencoder framework. The proposed method learns sparse data representations that consist of a linear combination of a small number of predetermined orthogonal atoms. The sparse coding problem is solved using a learnable version of the iterative shrinkage thresholding algorithm (ISTA). Experiments on two image datasets demonstrate that our model achieves improved image reconstruction results compared to state-of-the-art methods. Moreover, we demonstrate that the use of learned sparse code vectors allows us to perform downstream tasks like image generation and unsupervised image segmentation through clustering image patches.

1. Introduction

A major challenge towards applying artificial intelligence to the enormous amounts of unlabeled image data gathered worldwide is the ability to learn effective visual representations of data without supervision. Various unsupervised representation learning techniques based on vari-

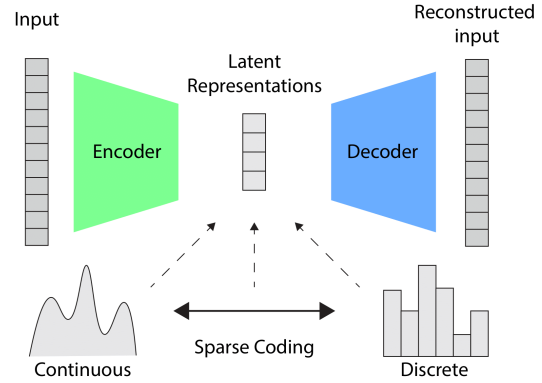


Figure 1: An illustration of using sparse coding to model the latent representations of VAEs. The majority of VAEs can be categorized into two classes based on whether the latent representations are continuous, using a static prior, or discrete, utilizing vector quantization (VQ) with a codebook. Combining the VAE framework with sparse coding can be conceptualized as representing the middle ground between continuous and discrete VAEs.

ational autoencoders (VAEs) [30] have been proposed to address this challenge. The primary objective of VAEs is to learn a mapping between high-dimensional observations and a lower dimensional representation space, such that the original observations can be approximately reconstructed from the lower-dimensional representation. These lower-dimensional visual representations allow for effectively training downstream tasks, such as image generation [23, 50], image segmentation [39] and clustering [54, 17].

Depending on the downstream task, different VAE variants have been proposed. These are distinguished by the assumptions they make about the world, which are encoded as meta-priors [4]. Based on this, two main classes of methods can be identified. The first class of methods [30, 23, 28, 9, 59, 32] learns representations with continuous latent variables (hereinafter referred to as continuous VAEs). These models utilized a static prior (usually a Gaussian distribution) to regularize the latent space so that disentangled representations and diverse new data can be gen-

erated. These approaches have demonstrated good disentanglement and generation performance for simple datasets [59, 28]. However, they typically suffer from several shortcomings when applied to complex datasets. First, the static prior makes the optimization process troublesome in practice because real world datasets cannot be simply modeled by a single distribution. Second, these methods tend to ignore the latent variables if the decoder is expressive enough to model the data distribution, resulting in posterior collapse [42]. Third, while the global structure of the input is well captured by latent representations, the more intricate local structure is not, leading to bad reconstructions.

The second class of methods [50, 15, 56, 34, 60] learns representations with discrete latent variables (hereinafter referred to as discrete VAEs). These methods typically utilize vector quantization (VQ) along with a codebook to learn a prior in the latent space. This approach not only circumvents issues of posterior collapse but has also been shown to achieve good image reconstruction and generation performance. Importantly, the perceptual quality of the reconstructed and generated samples may be further improved through the use of an adversarial or perceptual loss [26, 33]. However, discrete VAEs often require a large codebook to conserve the information of the encoded observations, which leads to the increase of model parameters and the codebook collapse problem [13]. Another shortcoming of discrete VAEs [50, 15, 56, 34] is that they tend to generate repeated artifactual patterns in the reconstructed image because the VQ operator uses the same quantization index to embed similar image patches. Moreover, the VQ operator does not allow the gradient to pass through the codebook. This makes the optimization process more challenging, as it requires the use of techniques such as the Gumbel-Softmax trick [25] or the straight-through estimator [5] to approximate the gradients.

To address aforementioned shortcomings, we introduce a new VAE variant SC-VAE, which stands for sparse coding-based VAE with learned ISTA [19]. Instead of using a fixed prior to learn continuous characteristics or utilizing VQ to learn discrete variables in the latent space, we propose to model latent representations as sparse linear combinations of atoms using sparse coding (SC) [45]. In the case of continuous VAEs, most of the latent factors are active at each time. In contrast, discrete VAEs require only one quantization index to be active at each time. SC-VAE adopts a middle ground, as is depicted in Figure 1. SC is anchored in the crucial realization that, despite the need for numerous variables to describe large collections of natural signals, individual instances can be effectively represented using only a small subset of these variables. This is in line with evidence [38] that biological vision systems, such as the visual cortex in mammals, process information as sparse signals.

In the field of computer vision, SC is a widely adopted

technique for efficiently reconstructing features or images [1, 41] and it has consistently demonstrated superior performance over VQ on benchmark recognition tasks [10, 55]. Therefore, we hypothesize that combining the VAE framework with sparse coding for latent representations reconstruction will lead to better reconstruction for the input. Moreover, prior works [43, 31] have indicated that incorporating orthogonality as a regularization method in VAEs is advantageous for promoting disentangled representations. SC-VAE offers a natural approach to acquire disentanglement by utilizing a predetermined orthogonal dictionary. Traditional algorithms for solving the sparse coding problem, such as Iterative Shrinkage-Thresholding Algorithm (ISTA) [11] and Fast Iterative Shrinkage-Thresholding Algorithm (FISTA) [3], can be easily integrated with VAE models. However, these algorithms do not allow to back-propagate gradients, which makes it impossible to train the model in an end-to-end manner. To mitigate this issue, a learnable version of ISTA [19] was used in this work.

Our contributions can be summarized as follows: (1) We introduce a new VAE variant, termed SC-VAE, which seamlessly integrates the VAE framework with sparse coding. The proposed SC-VAE is trainable in an end-to-end manner and does not suffer from posterior or codebook collapse. (2) We demonstrate that our method surpasses the performance of previous state-of-the-art approaches in image reconstruction tasks. Qualitative experiments reveal that our model exhibits superior generalization performance. (3) By training SC-VAE with a predetermined orthogonal dictionary, we illustrate the capacity to achieve effective disentanglement and smooth interpolation in generated images through the acquired sparse code vectors. (4) The learned sparse code vectors from SC-VAE demonstrate a capability for clustering of image patches. We highlight that this property enables us to achieve better unsupervised image segmentation performance than most state-of-the-art methods, coupled with robustness to noise.

2. Related Work

In this section, we delve into research closely related to SC-VAE. Earlier works on sparse coding-based VAEs [2, 16, 49, 47] primarily built upon the vanilla VAE framework [30]. These approaches achieved sparsity in latent variables by employing either specific prior distributions [2, 49, 47] or a learned threshold [16]. For example, sparse-coding variational auto-encoder (SVAE) [2] replaced the normal prior in the vanilla VAE with robust, sparsity-promoting priors (such as Laplace and Cauchy). However, it opted for a linear generator in the decoding process to reconstruct the input signal. This choice frequently resulted in suboptimal reconstruction outcomes due to the decoder’s limited expressive capacity. Variational sparse coding (VSC) model [49] focused on making the latent

space interpretable by enforcing sparsity using a mixture of Spike and Slab distributions. Variational sparse coding with learned thresholding (VSCLT) model [16] imposed sparsity through a shifted soft-threshold function. However, the non-differentiability of this function led to numerical instability. This issue arose as the function acted as a barrier to gradient flow from the generator to the inference network when a latent feature was unused. Sparsity-promoting dictionary model for variational autoencoders (SDM-VAE) [47] adopted a zero-mean Gaussian prior distribution with learnable variances as a sparsity regularizer. It used a fixed dictionary with unit-norm atoms to avoid scale ambiguity. As continuous VAEs, all these methods [2, 16, 49, 47] faced the inherent challenge of posterior collapse. To counteract this effect, VSC [49] implemented a Spike variable warm-up strategy to prevent posterior collapse. In contrast, the proposed SC-VAE explicitly learns sparse latent representations by combining the VAE framework with learned ISTA algorithm, avoiding the challenges of these prior works.

3. Preliminaries

In this section, we first briefly introduce the optimization framework of sparse coding. Then, we describe the algorithm unrolling version of ISTA (Learnable ISTA) [19] involved in our approach.

3.1. Sparse Coding

Let $X \in \mathbb{R}^n$ be an input vector, $Z \in \mathbb{R}^K$ be a sparse code vector and $\mathbf{D} \in \mathbb{R}^{n \times K}$ be a codebook matrix whose columns are atoms. The goal is to find an optimal way to reconstruct X based on a sparse linear combination of atoms in \mathbf{D} . Sparse coding typically involves minimizing the following energy function:

$$E_{\mathbf{D}}(X, Z) = \frac{1}{2} \|X - \mathbf{D}Z\|_2^2 + \alpha \|Z\|_1. \quad (1)$$

This energy function comprises two terms. The first term is a data term that penalizes differences between the input vector and its reconstruction as quantified by the $L2$ norm. The second term is an $L1$ norm, which acts as regularization to induce sparsity on the sparse code vector Z . α is a coefficient controlling the sparsity penalty.

3.2. Learnable ISTA

A popular algorithm for learning sparse codes is called ISTA [19], which iterates the following recursive equation to convergence:

$$Z(t+1) = h_{\theta}(W_e X + SZ(t)) \quad Z(0) = 0. \quad (2)$$

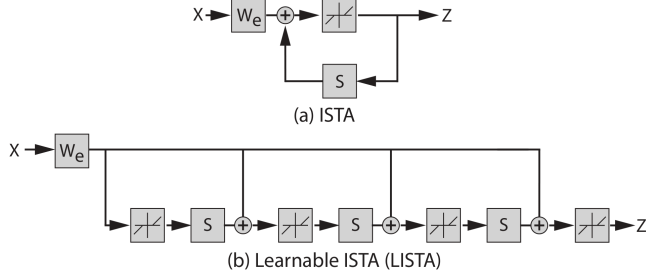


Figure 2: (a) The diagram of the ISTA algorithm for sparse coding. (b) The diagram of the Learnable ISTA, which is a time-unfolded version of the ISTA algorithm.

The elements in Eq. (2) are defined as follows:

$$\text{filter matrix: } W_e = \frac{1}{L} \mathbf{D}^\top$$

$$\text{mutual inhibition matrix: } S = I - \frac{1}{L} \mathbf{D}^\top \mathbf{D}$$

$$\text{shrinkage function: } [h_{\theta}(V)]_i = \text{sign}(V_i)(|V_i| - \theta_i)_+$$

Here, L is a constant, which is defined as an upper bound on the largest eigenvalue of $\mathbf{D}^\top \mathbf{D}$. Both the filter matrix and the mutual inhibition matrix depend on the codebook matrix \mathbf{D} . The function $h_{\theta}(V)$ is a component-wise vector shrinkage function with a vector of thresholds θ , where each element in θ is set to $\frac{\alpha}{L}$. In ISTA [11], the optimal sparse code is the fixed point of $Z(t+1) = h_{\theta}(W_e X + SZ(t))$. The block diagram is shown in Figure 2(a). In LISTA [19], W_e , S and θ are treated as parameters of a time-unfolded recurrent neural network, where S is shared over layers and the back-propagation algorithm can be performed over training samples. The number of rollout steps s and the codebook matrix \mathbf{D} in LISTA are predetermined. The block diagram of LISTA is shown in Figure 2(b).

4. Approach

The proposed SC-VAE model aims to encode an image into a series of latent vector representations and then to utilize sparse coding to generate sparse code vectors for these representations. These sparse code vectors can be subsequently decoded back to the reconstructed image with a fixed dictionary and a decoder network. The diagram of the proposed model is shown in Figure 3. We discuss the model formulation in Section 4.1 and the loss functions in Section 4.2.

4.1. Model Formulation

Formally, the input of SC-VAE is an image $x \in \mathbb{R}^{H \times W \times C}$, where H , W and C denote the height, width and the number of image channels, respectively. The image x goes first through an encoder E to obtain latent representations $E(x) \in \mathbb{R}^{h \times w \times n}$. Here, the values of h and w

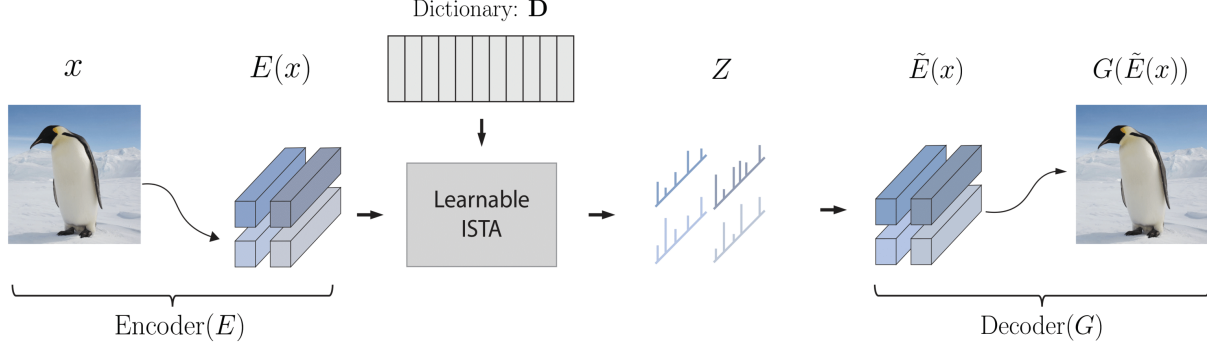


Figure 3: A schematic representation of the proposed Sparse Coding-VAE with Learned ISTA (SC-VAE). SC-VAE integrates a Learnable ISTA network within VAE framework to learn sparse code vectors in the latent space for the input image. Each image can be represented as one or several sparse code vectors, depending on the number of downsampling blocks in the encoding process.

depend on the number of downsampling blocks d in the encoder. Accordingly, these are defined as follows $h = \frac{H}{2^d}$ and $w = \frac{W}{2^d}$. n denotes the number of dimensions of each latent representation $E_{ij}(x)$, where $i \in [1, h]$ and $j \in [1, w]$. $E_{ij}^\top(x) \in \mathbb{R}^{n \times 1}$ is then given as an input to a Learnable ISTA network. The Learnable ISTA produces the sparse code vector $Z_{ij} \in \mathbb{R}^{1 \times K}$ for each $E_{ij}(x)$ by using the learnable parameters W_e , S and θ . Here, K denotes the number of atoms in the predetermined orthogonal dictionary \mathbf{D} . Each reconstructed latent representation $\tilde{E}_{ij}(x)$ can be calculated by the multiplication of Z_{ij} and \mathbf{D}^\top , which is then used to reconstruct the original image by going through a decoder neural network G . We denote the output of SC-VAE as $G(\tilde{E}(x))$.

4.2. Loss Functions

We need to define loss functions at two levels: the image level and the latent representation level. The loss in the image level should encourage our model to provide a good reconstruction for the input image. The loss in the latent space should allow us not only to obtain good latent representation reconstruction, but also to learn sparse codes.

Image reconstruction. The most common image reconstruction term utilized in VAE models is the $L2$ loss. The $L2$ loss is defined as

$$\mathcal{L}_{rec} = \|G(\tilde{E}(x)) - x\|_2^2. \quad (3)$$

Latent representation reconstruction. We aim to learn how to reconstruct each latent representation $E_{ij}(x)$ based on a linear combination of atoms in the fixed orthogonal dictionary \mathbf{D} . Accordingly, the loss function for the latent representation reconstruction is given by:

$$\mathcal{L}_{latent} = \sum_{ij} (\|E_{ij}^\top(x) - \mathbf{D}Z_{ij}^\top\|_2^2 + \alpha \|Z_{ij}^\top\|_1). \quad (4)$$

Similar to Eq. (1), this loss consists of two terms. The first term is a $L2$ norm to penalize differences between the latent representations of input images and their latent representation reconstructions. The second term imposes sparsity to each latent sparse code vector Z_{ij} . α controls the sparseness of the learned sparse code vectors Z .

Total loss. An intuitive way to build the total loss function would be to simply add \mathcal{L}_{rec} and \mathcal{L}_{latent} . However, this loss function will not allow us to learn a good image reconstruction due to the summation term in \mathcal{L}_{latent} . This is because each input image corresponds to $h \times w$ latent representations. As a consequence, the model will focus on learning good sparse code vectors for these latent representations and pay less attention on adequately optimizing \mathcal{L}_{rec} . To account for this factor, we introduce coefficients $\frac{1}{hw}$ to each of the latent representation $E_{ij}(x)$, which allows for appropriately balancing the two terms. Thus, the total loss for our model is the following:

$$\mathcal{L}_{SC-VAE}(E, G, W_e, S, \theta) = \mathcal{L}_{rec} + \frac{1}{hw} \mathcal{L}_{latent}. \quad (5)$$

5. Experiments

In this section, we first provide summaries of the datasets used to train the SC-VAE model and elaborate on the implementation details. Then, we demonstrate the effectiveness of SC-VAE under different problem settings, including 1) image reconstruction, 2) image generation through manipulating and interpolating learned sparse code vectors, 3) image patches clustering and 4) unsupervised image segmentation associated with its noise robustness analysis. Moreover, an ablation study for the influence of the number of rollout steps (s) in LISTA is provided.

Dataset. For our experiments, we used the Flickr-Faces-HQ (FFHQ) [27] and ImageNet [12] datasets. The FFHQ dataset comprises 70,000 images with a training set of

60,000 images and a validation set of 10,000 images. ImageNet is a widely used benchmark dataset for visual recognition tasks. It consists of 1.2 million training images and 50,000 validation images, with each image associated with one of 1,000 distinct categories. The images in both datasets are high-resolution and diverse, making them challenging for VAEs to model. All images were resized to 256×256 pixels.

Implementation Details. We adopted the encoder and decoder architecture of the VQGAN [15]. We trained SC-VAE models on the FFHQ and ImageNet datasets with four different number of downsampling blocks. The downsampling blocks d of the encoder were set to 3, 4, 6 and 8, resulting in 32×32 , 16×16 , 4×4 and 1×1 sparse code vectors in the latent space for an input image with a resolution of $256 \times 256 \times 3$. Moreover, the number of atoms in the dictionary, the number of rollout steps in LISTA and the dimension of latent vector representations were set to 512, 16 and 256, respectively. Discrete Cosine Transform (DCT) orthogonal matrix was used to generate the dictionary. The sparsity coefficient α was initialized to 1 and then updated during training. To optimize our SC-VAE model, the Adam [29] optimizer was used with a learning rate of 10^{-4} . The training ran for a total of 10 epochs and the batch size for each iteration was set to 16. We kept the models that achieved the lowest total loss for further evaluation. More detailed information about the architecture of SC-VAE along with a visualization of dictionary atoms can be found in the supplementary material.

5.1. Image Reconstruction

Baselines and Evaluation Metrics. Two sparse coding-based VAEs (VSC [49] and VSCLT [16]), three continuous VAE (Vanilla VAE [30], β -VAE [23], and Info-VAE [59]) and four discrete VAE models (VQGAN [15], ViT-VQGAN [56], RQ-VAE [34] and Mo-VQGAN [60]) were selected as our baselines. We used the same model architectures as the ones described in the respective papers. We evaluated the quality between reconstructed images and original images using four most common evaluation metrics (i.e., Peak Signal-to-Noise Ratio (PSNR), Structural Similarity Index Measure (SSIM), Learned Perceptual Image Patch Similarity (LPIPS) [58], and reconstructed Fréchet Inception Distance (rFID) [22]). PSNR measures the amount of noise introduced by the reconstruction process. SSIM quantifies the similarity between two images by taking into account not only pixel values, but also the structural and textural information in the images. LPIPS and rFID use a pre-trained deep neural network to measure the perceptual distance and distribution distance between two images, respectively.

Quantitative experimental results comparing the image reconstruction performance of SC-VAE with the baseline methods are listed in Table 1. We report the performance

Table 1: Quantitative reconstruction results on the validation sets of FFHQ [27] (10,000 images) and ImageNet [12] (50,000 images). \mathcal{C} and K denote the shape of latent codes and the cookbook size, respectively. \dagger , \ddagger , Υ and \wedge are used to distinguish the same method with different \mathcal{C} . The top two results across different metrics are highlighted in bold and red, respectively.

Model	Dataset	\mathcal{C}	K	PSNR \uparrow	SSIM \uparrow	LPIPS \downarrow	rFID \downarrow
VSC [49]	FFHQ	256	-	17.62	0.4458	0.6148	450.98
VSCLT [16]		256	-	12.97	0.3034	0.4426	249.54
Vanilla VAE [30]		256	-	18.00	0.4960	0.6568	178.17
β -VAE [23]		256	-	16.63	0.4763	0.6878	186.87
Info-VAE [59]		256	-	15.85	0.4560	0.6990	232.37
VQGAN [15]		$16 \times 16 \times 1$	1024	22.24	0.6641	0.1175	4.42
ViT-VQGAN [56]		$32 \times 32 \times 1$	8192	-	-	-	3.13
RQ-VAE † [34]		$8 \times 8 \times 4$	2048	22.99	0.6700	0.1302	7.04
RQ-VAE ‡ [34]		$16 \times 16 \times 4$	2048	24.53	0.7602	0.0895	3.88
Mo-VQGAN [60]		$16 \times 16 \times 4$	1024	26.72	0.8212	0.0585	2.26
SC-VAE †		$1 \times 1 \times 1$	512	17.25	0.4946	0.7177	195.30
SC-VAE ‡		$4 \times 4 \times 1$	512	22.29	0.6110	0.4907	115.91
SC-VAE $^\Upsilon$		$16 \times 16 \times 1$	512	29.70	0.8347	0.1956	41.56
SC-VAE $^\wedge$		$32 \times 32 \times 1$	512	34.92	0.9497	0.0080	4.21
VSC [49]	ImageNet	256	-	17.76	0.5534	0.5999	454.75
VSCLT [16]		256	-	12.70	0.3016	0.7578	336.72
Vanilla VAE [30]		256	-	17.88	0.4441	0.6957	163.00
β -VAE [23]		256	-	16.10	0.4165	0.7142	224.03
Info-VAE [59]		256	-	17.20	0.4259	0.7097	178.94
VQGAN † [15]		$16 \times 16 \times 1$	1024	19.47	0.5214	0.1950	6.25
VQGAN ‡ [15]		$16 \times 16 \times 1$	16384	19.93	0.5424	0.1766	3.64
ViT-VQGAN [56]		$8 \times 8 \times 4$	2048	-	-	-	1.28
RQ-VAE [34]		$8 \times 8 \times 4$	2048	20.76	0.5416	0.1381	4.73
Mo-VQGAN [60]		$16 \times 16 \times 4$	1024	22.42	0.6731	0.1132	1.12
SC-VAE †		$1 \times 1 \times 1$	512	16.86	0.4306	0.8163	185.68
SC-VAE ‡		$4 \times 4 \times 1$	512	23.04	0.5906	0.5081	114.08
SC-VAE $^\Upsilon$		$16 \times 16 \times 1$	512	30.74	0.8594	0.1447	23.23
SC-VAE $^\wedge$		$32 \times 32 \times 1$	512	38.40	0.9688	0.0070	0.71

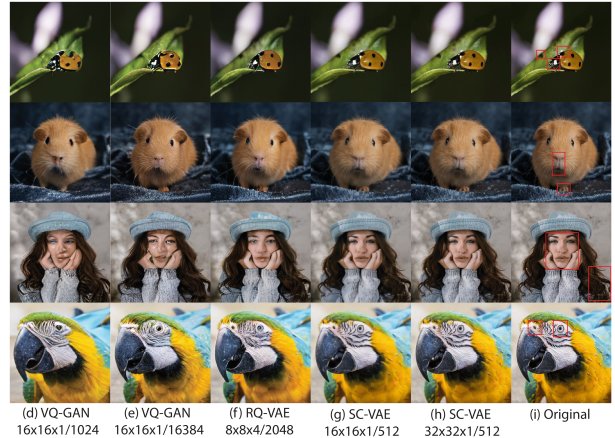


Figure 4: Image reconstructions from different models trained on ImageNet dataset. Original images in the top two rows are from the validation set of ImageNet dataset. Two external images are shown in the last two rows to demonstrate the generalizability of different methods. The numbers denote the shape of latent codes and learned codebook (dictionary) size, respectively. SC-VAE achieved improved image reconstruction compared to the baselines. Zoom in to see the details of the red square area.

of our model with four different downsampling blocks ($d = 3, 4, 6, 8$). The top two results across different metrics are

highlighted in bold and red, respectively. As can be seen in the Table 1, SC-VAE significantly improved the image quality compared to other methods in terms of PSNR, SSIM and LPIPS scores in the FFHQ dataset and in terms of all scores in the ImageNet dataset when the shape of latent codes was set to $32 \times 32 \times 1$. Even after downsampling the original image to a shape of $16 \times 16 \times 1$, our approach significantly outperformed other methods in terms of PSNR and SSIM scores on both datasets. With increasing number of downsampling blocks, our model struggled with image reconstruction.

Among baseline methods, sparse coding-based VAEs (i.e. VSC [49] and VSCLT [16]) and continuous VAEs (i.e. Vanilla VAE [30], β -VAE [23], and Info-VAE [59]) produced poor reconstructions of the original images. This is because both FFHQ and ImageNet datasets exhibit a significant amount of diversity in terms of objects and background, which is challenging to model with a static prior distribution in the latent space. Discrete VAEs (i.e. VQGAN [15], ViT-VQGAN [56], RQ-VAE [34] and Mo-VQGAN [60]) demonstrated better performance compared to continuous VAEs. However, they produced lower PSNR and SSIM scores compared to our model. That might be because the adversarial training and perceptual loss of discrete VAEs force the model to generate more visually appealing and realistic outputs without paying sufficient attention to structural information. Furthermore, these models used a much larger codebook size than ours. The codebook collapse problem caused by the larger codebook might make it difficult for them to reconstruct detailed and accurate information.

Four images and paired reconstructed results from different models were visualized in Figure 4. The models used to reconstruct these images are trained on the training set of ImageNet dataset. The absence of official code and pre-trained models prevents us from providing results for ViT-VQGAN and Mo-VQGAN. We present visualizations from unofficial implementation of ViT-VQGAN in the supplementary materials for reference. As for sparse coding and continuous VAEs, we refrained from presenting their visualizations due to their subpar reconstruction capabilities. As is shown in the Figure 4, VQGAN, RQ-VAE and our models accomplished visually appealing outcomes. The original images in the first two rows were randomly selected from the validation set of ImageNet. VQGAN tended to generate repeated artifacts on similar semantic patches, such as the leaves and noses. While RQ-VAE enhanced the visual aspect, it struggled to accurately reconstruct intricate details and complex patterns. In contrast to these models, SC-VAE generated much more authentic-looking details without suffering from any of the aforementioned shortcomings. The original images in the last two rows are part of the external images of ImageNet dataset. They were used to test

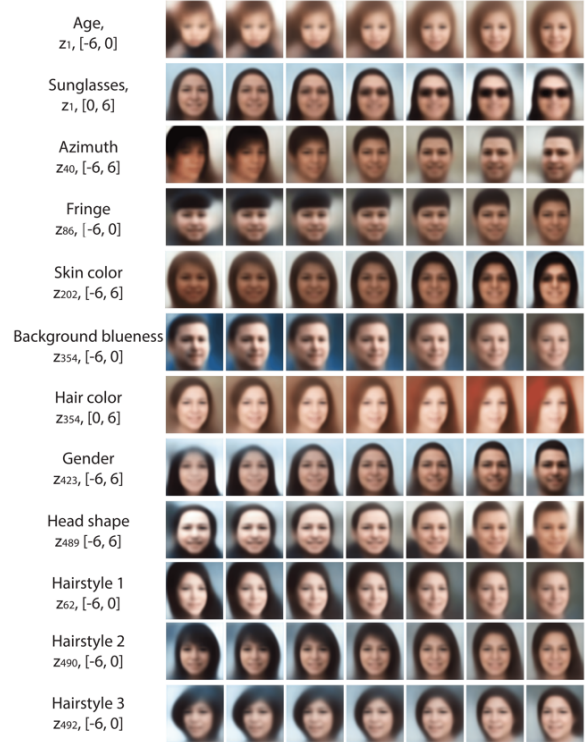


Figure 5: Manipulating sparse code vectors on FFHQ. Each row represents a different seed image used to infer the latent sparse code vector in the SC-VAE[†] model. The disentangled attributes associated with the i -th component of a sparse code vector z and a traversal range are shown in the first column.

the generalizability of different models. SC-VAE was able to accurately identify and reconstruct patterns that have not previously been encountered. However, the reconstructed images from VQGAN and RQVAE did not preserve the detailed information and distorted the original images.

5.2. Image Generation

In this section, we explore whether utilizing a pre-defined orthogonal DCT matrix in the SC-VAE model enables the generation of images by manipulating and interpolating sparse code vectors.

Manipulating sparse code vectors. Quantifying feature disentanglement in natural data is challenging since the source features are typically unknown. Nevertheless, as in the approach of [28], we can assess the impact of altering individual components of a sparse code vector on the generated samples qualitatively. To this end, we used the SC-VAE[†] model with a downsampling block of 8 trained on the FFHQ dataset. We selected examples from the validation set, manipulated individual dimensions within the sparse code vectors, and then produced samples based on

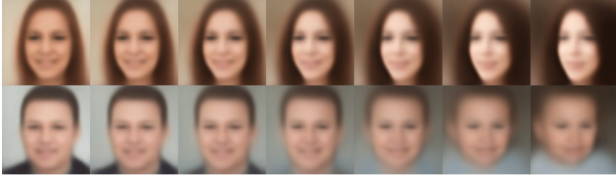


Figure 6: Interpolation between the sparse code vectors of two samples from the SC-VAE[†] model trained on FFHQ.

these modified latent sparse vectors. We found that 10 components of the dimensions exploited by the SC-VAE[†] model controlled interpretable aspects in the generated data, as is shown in Figure 5.

Interpolating sparse code vectors. Figure 6 shows smooth interpolation between the latent sparse code vectors of two images generated by SC-VAE[†]. Additional manipulation and interpolation results can be found in the supplementary material.

5.3. Image Patches Clustering

The latent sparse code vectors learned by SC-VAE can be thought of as compressed representations of the input image. To better interpret the learned sparse code vectors, we aligned each of them with a corresponding patch of the input image. Image patch clustering was then performed based on these sparse code vectors. We examined one pre-trained SC-VAE^Y model on FFHQ dataset with a downsampling block of $d = 4$. 1,000 images were randomly selected from the validation set, resulting in 256,000 pairs of image patches with a resolution of $16 \times 16 \times 3$ and sparse code vectors with a dimension of 512. The sparse code vectors were clustered into 1,000 groups using the K-means clustering algorithm. We randomly selected 15 groups and 40 patches from each group to visualize the clustering results. As can be seen in Figure 7, image patches with similar patterns were grouped together. More clustering results on the validation set of FFHQ and ImageNet datasets can be found in the supplementary material.

5.4. Unsupervised Image Segmentation

This section investigates whether the sparse code vectors estimated by our models enable us to conduct image segmentation tasks without supervision.

Qualitative analysis. We utilized two SC-VAE^Λ models that were pre-trained on the training set of the FFHQ and ImageNet datasets, respectively. These models had a downsampling block of $d = 3$. The images were transformed into sparse code vectors with a size of $32 \times 32 \times 1$ using the encoder and LISTA network of the SC-VAE^Λ. Afterwards, the K-means algorithm was applied to cluster these sparse code vectors into 5 categories, generating a 32×32 mask with 5 different classes for each image. The segmentation

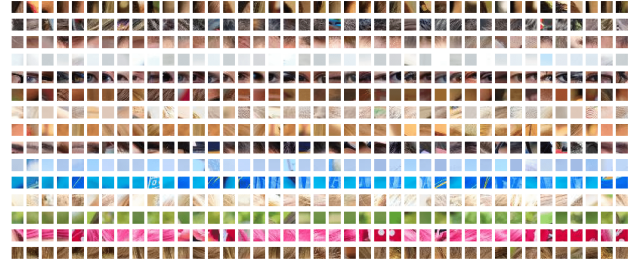


Figure 7: 15 randomly selected image patch clusters generated by clustering the learned sparse code vectors of SC-VAE^Y using the K-means algorithm. Each row represents one cluster. Image patches with similar patterns were grouped together.



Figure 8: Unsupervised image segmentation results. **Top:** images from the validation set of FFHQ. **Bottom:** images from the validation set of ImageNet.

results were visualized in Figure 8. The faces and objects in the images were successfully detected and segmented by simply grouping the patch-level sparse codes using the K-means algorithm.

Quantitative comparisons to prior work. We evaluated the SC-VAE^Λ model pre-trained on ImageNet dataset on Flowers [37], Caltech-UCSD Birds-200-2011 (CUB) [51] and International Skin Imaging Collaboration 2016 (ISIC-2016) [20] datasets. We followed [48] to generate the test set and the ground-truth masks of Flowers [37] and CUB [51]. To achieve unsupervised image segmentation results, we initially applied a spectral clustering algorithm to group the sparse code vectors into 2 or 3 classes per image. Subsequently, we utilized boundary connectivity information [61] to determine whether each class corresponds to the foreground or background. We compared the performance of our method to prior works (see Table 2). Note that this is not a fair comparison. Most of the methods we compare to, excluding GrabCut [44] and IEM [48], require a training set with a distribution identical to that of the test set for model

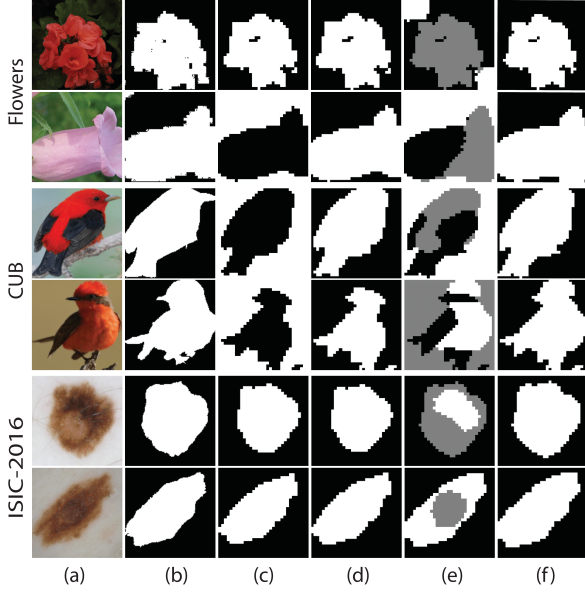


Figure 9: Unsupervised image segmentation results of SC-VAE[^] on Flowers [37], CUB [51] and ISIC-2016 [20]. *Left to right:* (a) input image. (b) ground truth mask. (c) and (e) segmentation results by clustering sparse code vectors per image into 2 or 3 clusters using a spectral clustering algorithm. (d) and (f) boundary connectivity information [61] was used to decide the foreground and the background.

training. In contrast, our pre-trained SC-VAE[^] model can segment an image without the need for fine-tuning on Flower [37], CUB [51] and ISIC-2016 [20] datasets. Interestingly, our model performed better than most of the baselines, which used more sophisticated approaches for segmentation, such as adversarial training [6, 8, 21, 57, 14] and attention mechanisms [35]. We attribute the superior performance of SC-VAE[^] over the baselines to its capability to learn meaningful and distinct sparse representations. This ability enables SC-VAE[^] to learn relationships between patches effectively. Several qualitative results of SC-VAE[^] on Flower [37], CUB [51] and ISIC-2016 [20] datasets are shown in Figure 9. More qualitative results can be found in the supplementary material.

Noise robustness analysis. Sparse coding has been extensively applied for image denoising tasks. We investigate whether the pretrained SC-VAE[^] exhibits resilience to noise in the unsupervised image segmentation task. To evaluate this, we added independent and identically distributed (i.i.d.) Gaussian noise with zero mean and various levels of noise σ to each image in the test set of CUB dataset and compared its performance with three baselines (ReDO [8], DRC [57], and DS-ComGAN [14]), which have been pre-trained on the training set of CUB dataset. The performance of other baselines was not shown due to the unavailability

Table 2: Unsupervised segmentation results on Flowers [37] and CUB [51], measured in terms of IoU and DICE scores. SC-VAE[^] was compared with state-of-the-art unsupervised and weakly supervised segmentation methods. * denotes a GAN-based model. OneGAN[◇] is a weakly supervised baseline that relies on clean backgrounds as additional input. The best results across different metrics and datasets are highlighted in bold.

Methods	Flowers		CUB		ISIC-2016	
	IoU \uparrow	DICE \uparrow	IoU \uparrow	DICE \uparrow	IoU \uparrow	DICE \uparrow
GrabCut [44]	69.2	79.1	36.0	48.7	-	-
W-Net [53]	74.3	83.0	24.8	38.9	31.8	44.4
ReDO* [8]	77.8	85.3	43.5	56.8	20.1	29.1
IODINE [18]	32.6	46.0	30.9	44.6	31.9	42.4
PerturbGAN* [7]	-	-	38.0	-	-	-
OneGAN [◇] * [6]	-	-	55.5	69.2	-	-
Slot-Attn [35]	32.9	45.7	35.6	51.5	22.2	32.8
IEM [48]	76.8	84.6	52.2	66.0	65.5	75.1
DRC [57]	46.9	60.8	56.4	70.9	44.1	56.4
DS-ComGAN* [14]	76.9	83.1	60.7	71.3	43.9	57.8
SC-VAE [^] (2 classes)	81.2	88.5	53.2	67.6	61.6	70.7
SC-VAE [^] (3 classes)	67.3	78.6	58.2	72.1	60.8	71.5

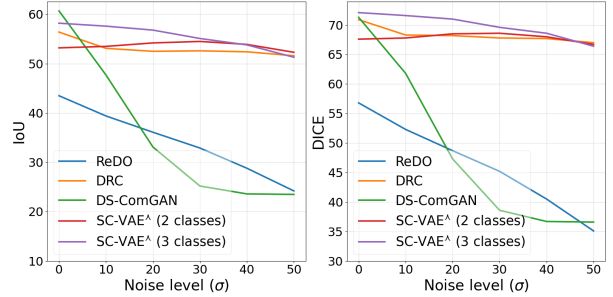


Figure 10: Noise robustness analysis. We show the unsupervised segmentation results of SC-VAE[^] and three baselines on CUB [51] at different levels of noise σ .

ity of pretrained models. As depicted in Figure 10, both SC-VAE[^] and DRC [57] demonstrated robustness against Gaussian noise whereas the performance of ReDO [8] and DS-ComGAN [14] noticeably declined as the noise level increased. DRC [57] includes Total Variation norm [46] within its loss function, which potentially explains the robustness to noise it exhibited.

5.5. Ablation Study

We conducted an ablation study to analyze the influence of the number of rollout steps (s) in LISTA on the reconstruction ability of SC-VAE. We trained the SC-VAE[^] model ($d = 4$) with different s and reported the quantitative results in Table 3. The sparsity of the learned sparse code vectors was calculated using the Hoyer metric [24]. We reported the average sparsity and four reconstruction metrics among the validation set of FFHQ dataset. Sparsity first decreased and then increased as s increased. Lower sparsity corresponds to better reconstruction outcomes.

Table 3: Quantitative reconstruction results of SC-VAE ($d = 4$) with different number of rollout steps s .

Model	Sparsity	PSNR \uparrow	SSIM \uparrow	LPIPS \downarrow	rFID \downarrow
SC-VAE ($s = 1$)	89.5%	27.30	0.7603	0.3039	71.17
SC-VAE ($s = 5$)	71.9%	31.13	0.8759	0.1279	30.07
SC-VAE ($s = 10$)	75.1%	31.05	0.8771	0.1261	29.50
SC-VAE ($s = 15$)	74.9%	31.41	0.8815	0.1155	28.11
SC-VAE ($s = 20$)	80.9%	30.66	0.8656	0.1451	32.87
SC-VAE ($s = 25$)	81.5%	30.59	0.8693	0.1373	30.45
SC-VAE ($s = 30$)	83.2%	29.71	0.8369	0.1925	41.89

6. Conclusion

In this paper, we introduced a novel variant of VAE, which we refer to as SC-VAE. Our approach harnesses a learned ISTA algorithm to learn latent sparse representations for input images. The utilization of SC-VAE facilitates the smooth flow of gradients through the network, effectively addressing limitations present in existing VAE models. Through our experiments, we showcased the superior performance of SC-VAE compared to well-established baseline methods in image reconstruction. Furthermore, we illustrated that SC-VAE can generate new images through manipulating and interpolating sparse code vectors. Moreover, SC-VAE’s ability to learn relationship between image patches enabled us to perform unsupervised image segmentation, coupled with its resilience to noise.

SC-VAE: Sparse Coding-based Variational Autoencoder with Learned ISTA

Supplementary Material

The supplementary material for our work *SC-VAE: Sparse Coding-based Variational Autoencoder with Learned ISTA* is structured as follows: Section 1 details the encoder and decoder architecture of the SC-VAE model. In Section 2, the dictionary atoms are visualized. In Section 3, we provide the training losses on the ImageNet dataset when varying the number of downsampling (upsampling) blocks (d) in the encoder (decoder) of the SC-VAE model. In Section 4, the visualized reconstruction results of an unofficial implementation of VIT-VQGAN [56] are provided. We provide additional manipulation and interpolation results on the FFHQ dataset in Section 5, while additional clustering results of image patches on both FFHQ and ImageNet are provided in Section 6. Supplementary unsupervised image segmentation results are given in Section 7.

1. The Encoder and Decoder Architecture of SC-VAE

The SC-VAE model’s encoder and decoder architecture mirrors that of VQGAN [15]. Details about the architecture are provided in Table 4. H , W and C denote the height, width and the number of channels of an input image, respectively. C' and C'' represent the number of channels of the feature maps that are produced as outputs by the intermediate layers of the encoder and decode network. In our experiment, C' and C'' were set to 128 and 512, respectively. n denotes the number of dimensions of each latent representation, which was set to 256. The variable d represents the number of blocks used for downsampling and upsampling. Therefore, we can calculate the height (h) and width (w) of the encoder’s output feature maps by dividing the height (H) and width (W) of input images by 2 raised to the power of d .

2. Visualization of Dictionary Atoms

Figure 11 demonstrates the 512 columns (atoms) of the pre-determined Discrete Cosine Transform (DCT) dictionary. Each atom is of dimension 256, which corresponds to the size of 16×16 images when shaped.

3. Training Losses

Figures 12, 13, 14 and 15 show the training losses over 120,000 training steps on the ImageNet dataset. The number of downsampling (upsampling) blocks (d) in the encoder (decoder) of the SC-VAE model are 3, 4, 6 and 8, respectively. As depicted in these figures, the LISTA net-

Table 4: High-level architecture of the encoder and decoder of the SC-VAE model. H , W , and C refer to the height, width, and the number of channels of an input image. C' and C'' represent the number of channels of the feature maps from intermediate layers in the encoder and decoder networks. n denotes the number of dimensions of each latent representation, while d represents the number of downsampling (upsampling) blocks. Note that $h = \frac{H}{2^d}$, $w = \frac{W}{2^d}$.

Encoder	$x \in \mathbb{R}^{H \times W \times C}$
	2D Convolution $\rightarrow \mathbb{R}^{H \times W \times C'}$
	$d \times \{\text{Residual Block, Downsample Block}\} \rightarrow \mathbb{R}^{h \times w \times C''}$
	Residual Block $\rightarrow \mathbb{R}^{h \times w \times C''}$
	Non-Local Block $\rightarrow \mathbb{R}^{h \times w \times C''}$
	Residual Block $\rightarrow \mathbb{R}^{h \times w \times C''}$
	Group Normalization [52] $\rightarrow \mathbb{R}^{h \times w \times C''}$
	Swish Activation Function [40] $\rightarrow \mathbb{R}^{h \times w \times C''}$
Decoder	2D Convolution $\rightarrow E(x) \in \mathbb{R}^{h \times w \times n}$
	$\tilde{E}(x) \in \mathbb{R}^{h \times w \times n}$
	2D Convolution $\rightarrow \mathbb{R}^{h \times w \times C''}$
	Residual Block $\rightarrow \mathbb{R}^{h \times w \times C''}$
	Non-Local Block $\rightarrow \mathbb{R}^{h \times w \times C''}$
	Residual Block $\rightarrow \mathbb{R}^{h \times w \times C''}$
	$d \times \{\text{Residual Block, Upsample Block}\} \rightarrow \mathbb{R}^{H \times W \times C'}$
	Group Normalization [52] $\rightarrow \mathbb{R}^{H \times W \times C'}$
	Swish Activation Function [40] $\rightarrow \mathbb{R}^{H \times W \times C'}$
	2D Convolution $\rightarrow G(\tilde{E}(x)) \in \mathbb{R}^{H \times W \times C}$

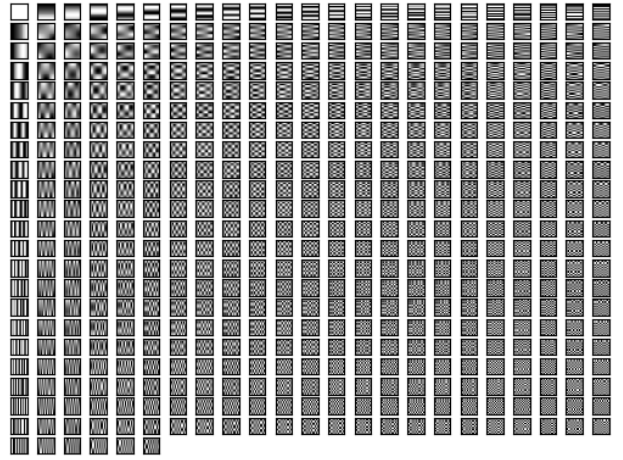


Figure 11: 512 atoms of the Discrete Cosine Transform (DCT) dictionary. All atoms were reshaped into a 16×16 image.

works within the SC-VAE models consistently converge to a stable point regardless of the chosen downsampling (up-

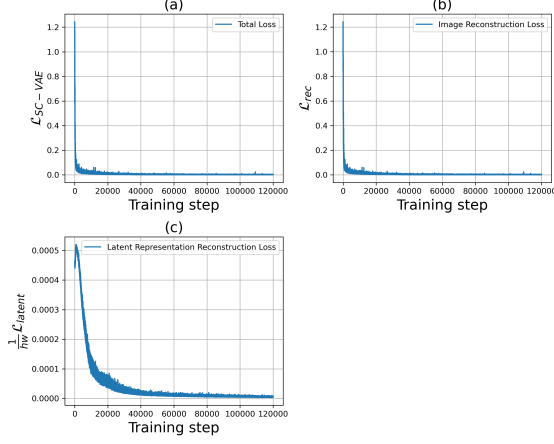


Figure 12: The training losses over 120,000 training steps on the ImageNet dataset. The number of downsampling (upsampling) blocks (d) in the encoder (decoder) of the SC-VAE model was set to 3 and the height (h) and width (w) of latent representations were 32. (a) Total loss \mathcal{L}_{SC-VAE} . (b) Image reconstruction loss \mathcal{L}_{rec} . (c) The mean of latent representations reconstruction loss $\frac{1}{hw}\mathcal{L}_{latent}$.

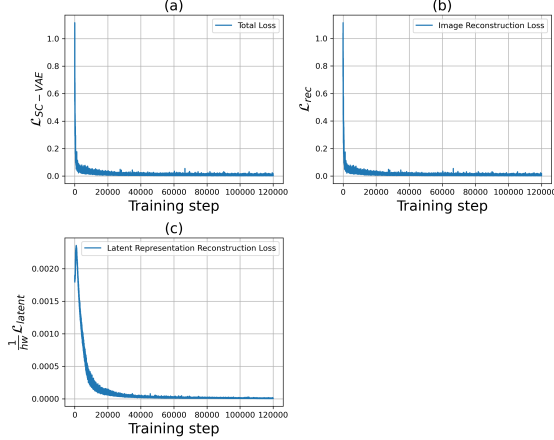


Figure 13: The training losses over 120,000 training steps on the ImageNet dataset. The number of downsampling (upsampling) blocks (d) in the encoder (decoder) of the SC-VAE model was set to 4 and the height (h) and width (w) of latent representations were 16. (a) Total loss \mathcal{L}_{SC-VAE} . (b) Image reconstruction loss \mathcal{L}_{rec} . (c) The mean of latent representations reconstruction loss $\frac{1}{hw}\mathcal{L}_{latent}$.

sampling) block d . However, increasing d leads to worse image reconstructions (\mathcal{L}_{rec}) in SC-VAE.

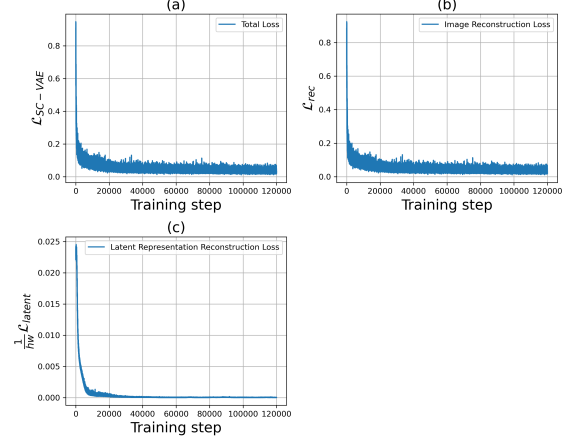


Figure 14: The training losses over 120,000 training steps on the ImageNet dataset. The number of downsampling (upsampling) blocks (d) in the encoder (decoder) of the SC-VAE model was set to 6 and the height (h) and width (w) of latent representations were 4. (a) Total loss \mathcal{L}_{SC-VAE} . (b) Image reconstruction loss \mathcal{L}_{rec} . (c) The mean of latent representations reconstruction loss $\frac{1}{hw}\mathcal{L}_{latent}$.

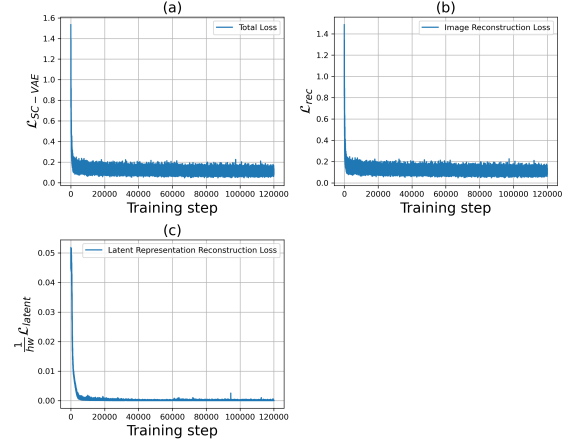


Figure 15: The training losses over 120,000 training steps on the ImageNet dataset. The number of downsampling (upsampling) blocks (d) in the encoder (decoder) of the SC-VAE model was set to 8 and the height (h) and width (w) of latent representations were 1. (a) Total loss \mathcal{L}_{SC-VAE} . (b) Image reconstruction loss \mathcal{L}_{rec} . (c) The mean of latent representations reconstruction loss $\frac{1}{hw}\mathcal{L}_{latent}$.

4. Image Reconstruction

Reconstruction results from unofficial implementation¹ of VIT-VQGAN [56] are presented in Figure 16. VIT-VQGAN [56] achieved visually appealing results. How-

¹<https://github.com/thuanz123/enhancing-transformers>

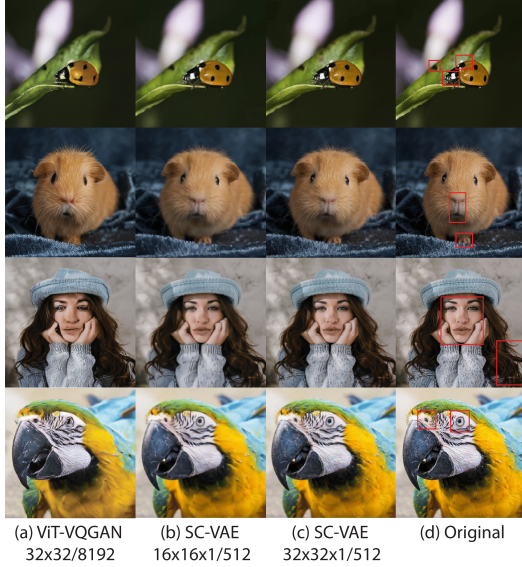


Figure 16: Image reconstructions from an unofficial implementation of VIT-VQGAN [56] and the SC-VAE models trained on ImageNet dataset. Original images in the top two rows are from the validation set of ImageNet dataset. Two external images are shown in the last two rows to demonstrate the generalizability of different methods. The numbers denote the shape of latent codes and the learned codebook (dictionary) size, respectively. SC-VAE achieved improved image reconstruction compared to VIT-VQGAN [56]. Zoom in to see the details in the red square area.

ever, similar to VQ-GAN [15] and RQ-VAE [34], it faced challenges in accurately reconstructing intricate details and complex patterns. Additionally, its generalization performance was inferior to that of our model.

5. Image Generation

Additional interpolation and manipulation results can be found in Figures 17 and 18, respectively.

6. Image Patches Clustering

Figures 19 and 20 showcase additional qualitative results of image patches clustering on FFHQ and ImageNet datasets, respectively. These results were obtained utilizing the pre-trained SC-VAE^Y model specific to each dataset with a downsampling block $d = 4$.

7. Unsupervised Image Segmentation

7.1. Qualitative Analysis on FFHQ and ImageNet

Additional qualitative unsupervised image segmentation results on the FFHQ and ImageNet datasets can be found

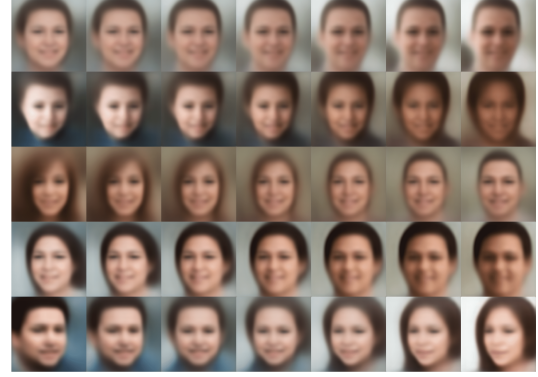


Figure 17: Interpolation between the sparse code vectors of two samples from the SC-VAE⁺ model trained on FFHQ.

in Figures 21 and 22, respectively. We utilized two SC-VAE⁺ models pre-trained on the training sets of FFHQ and ImageNet, each employing a downsampling block $d = 3$.

7.2. Quantitative comparisons to prior work

Figure 23 displays additional qualitative results from the Flowers [37] and Caltech-UCSD Birds-200-2011 (CUB) [51] datasets.

7.2.1 Evaluation Metrics

Intersection of Union (IoU). The IoU score quantifies the overlap between two regions. This is achieved by evaluating the ratio of their intersection to their union.

$$\text{IoU}(A, B) = \frac{|A \cap B|}{|A \cup B|}.$$

A denotes the ground-truth mask, while B denotes the inferred mask.

DICE score. Similarly, the DICE score is defined as:

$$\text{Dice}(A, B) = \frac{2|A \cap B|}{|A| + |B|}.$$

Higher is better for both scores.

7.2.2 Dataset Details

Flowers. The Flowers [37] dataset consists of 8,189 images across 102 different flower classes. Additionally, it includes segmentation masks generated by an automated algorithm designed explicitly for color photograph flower segmentation [36]. The dataset contains images that exhibit substantial variations in scale, pose, and lighting. Flowers [37] contains 1,020 test images.

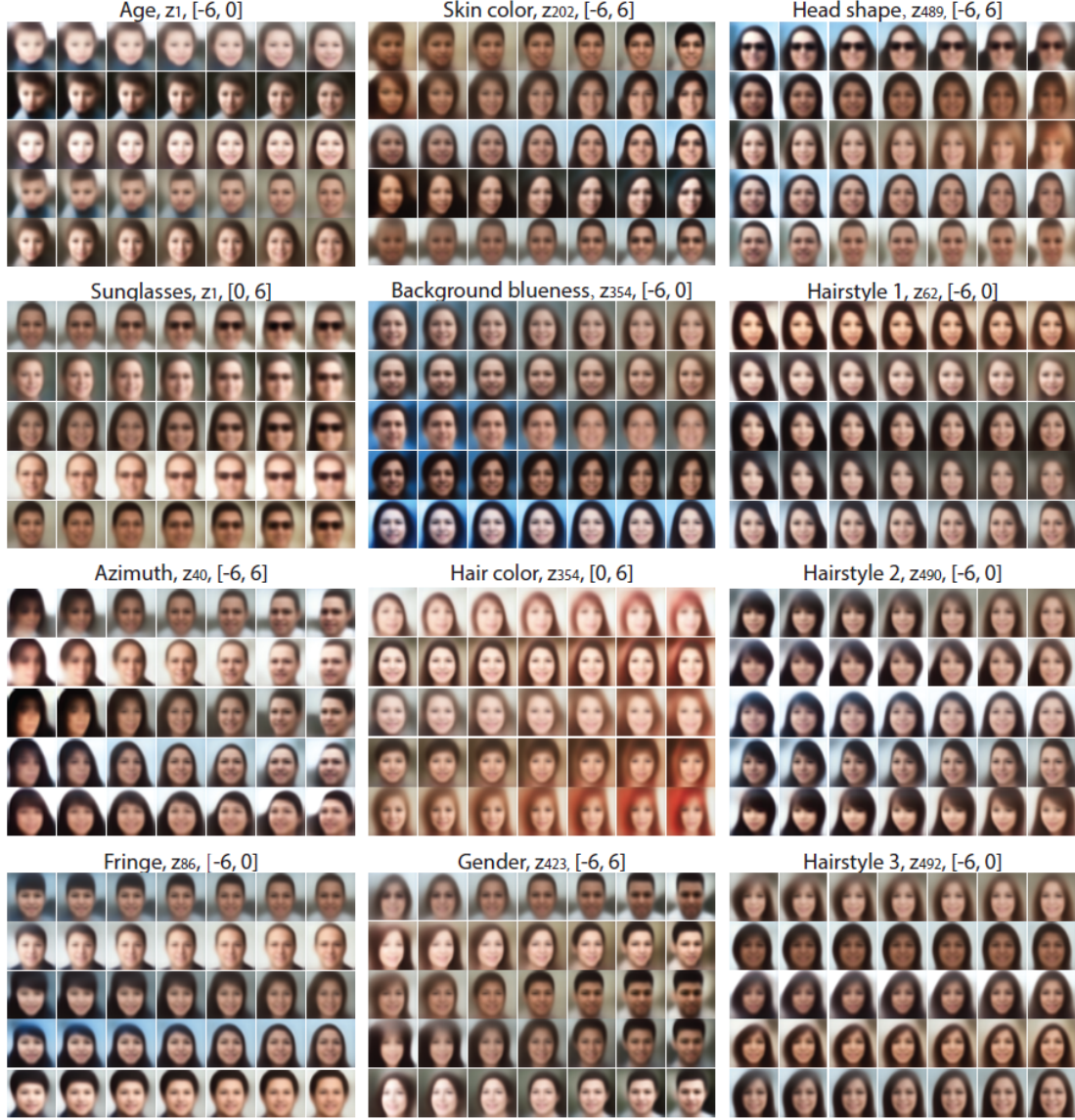


Figure 18: Manipulating sparse code vectors on FFHQ. Each block contains five seed images used to infer the latent sparse code vector in the SC-VAE[†] model. The disentangled attributes associated with the i -th component of a sparse code vector z and a traversal range are shown on the top of each block.

CUB. The CUB [51] dataset contains 11,788 images covering 200 bird classes, along with their segmentation masks. Every image comes with annotations for 15 part locations, 312 binary attributes, and 1 bounding box. We utilized the given bounding box to crop a central square from the image. The CUB dataset includes 1,000 test images.

ISIC-2016. The ISIC-2016 [20] dataset is a public challenge dataset dedicated to Skin Lesion Analysis for Melanoma Detection. Derived from the extensive International Skin Imaging Collaboration (ISIC) archive, it represents a significant collection of meticulously curated dermoscopic images of skin lesions. Within this challenge, a

subset of 900 images is designated as training data, while 379 images serve as testing data, aiming to provide representative samples for analysis.

For our experiments, we resized the input images into a resolution of 256×256 . Subsequently, we generated a binary mask of size 32×32 per image by employing the pre-trained SC-VAE[^] on the ImageNet dataset, along with a spectral clustering algorithm and boundary connectivity information [61]. To compute the IoU and DICE scores, both the inferred binary mask and the ground truth mask were resized to 128×128 .



Figure 19: 50 randomly selected image patch clusters from the validation set of the FFHQ dataset generated by clustering the learned sparse code vectors of the pre-trained SC-VAE^Y model using the K-means algorithm. Each row represents one cluster. Image patches with similar patterns were grouped together.



Figure 20: 50 randomly selected image patch clusters from the validation set of the ImageNet dataset generated by clustering the learned sparse code vectors of the pre-trained SC-VAE^Y model using the K-means algorithm. Each row represents one cluster. Image patches with similar patterns were grouped together.



Figure 21: Additional unsupervised image segmentation results. These results were generated by grouping sparse code vectors into 5 categories per image, utilizing the pre-trained SC-VAE⁺ model and the K-means algorithm. Images are from the validation set of the FFHQ dataset.

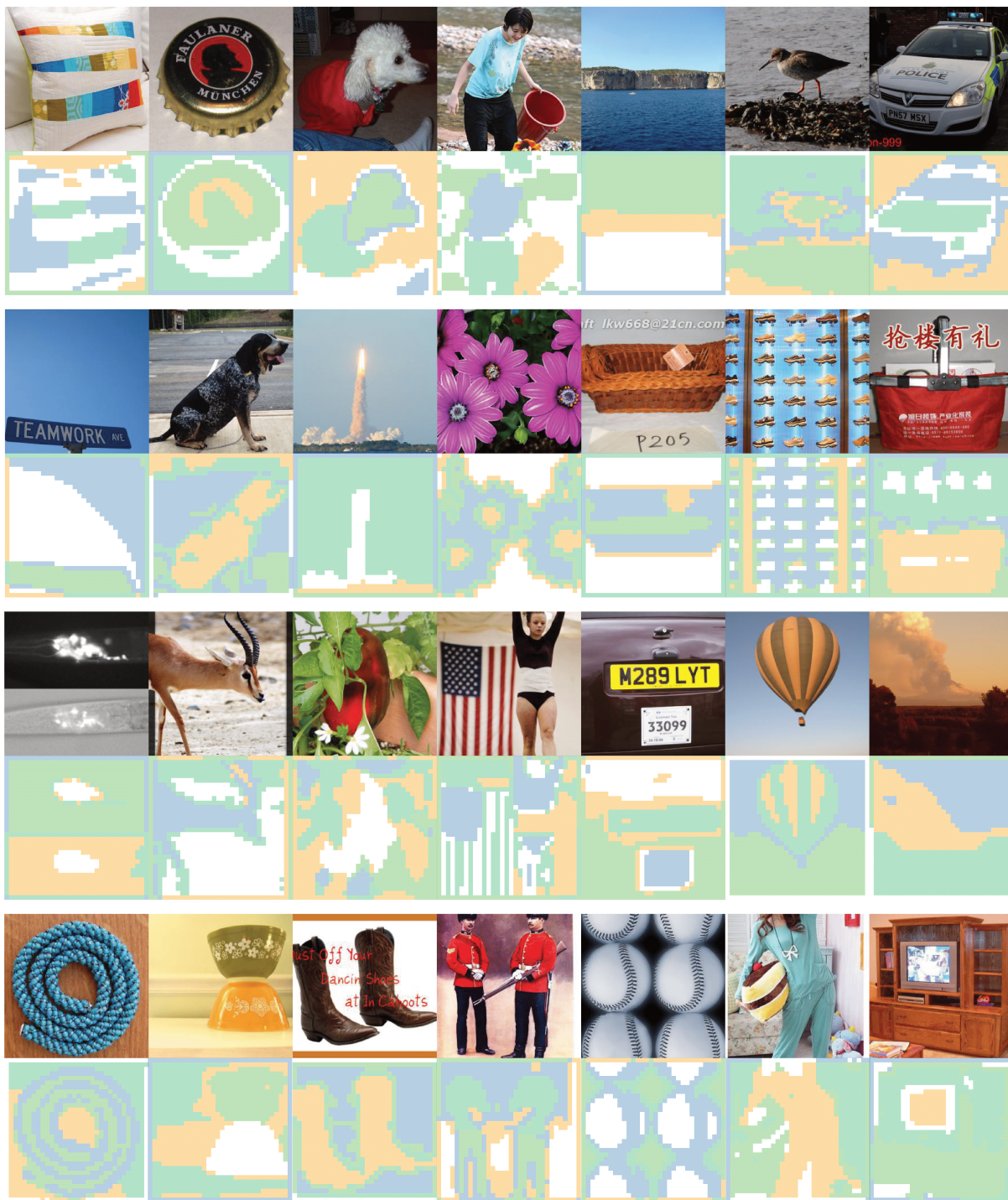


Figure 22: Additional unsupervised image segmentation results. These results were generated by grouping sparse code vectors into 5 categories per image, utilizing the pre-trained SC-VAE⁺ model and the K-means algorithm. Images are from the validation set of the ImageNet dataset.

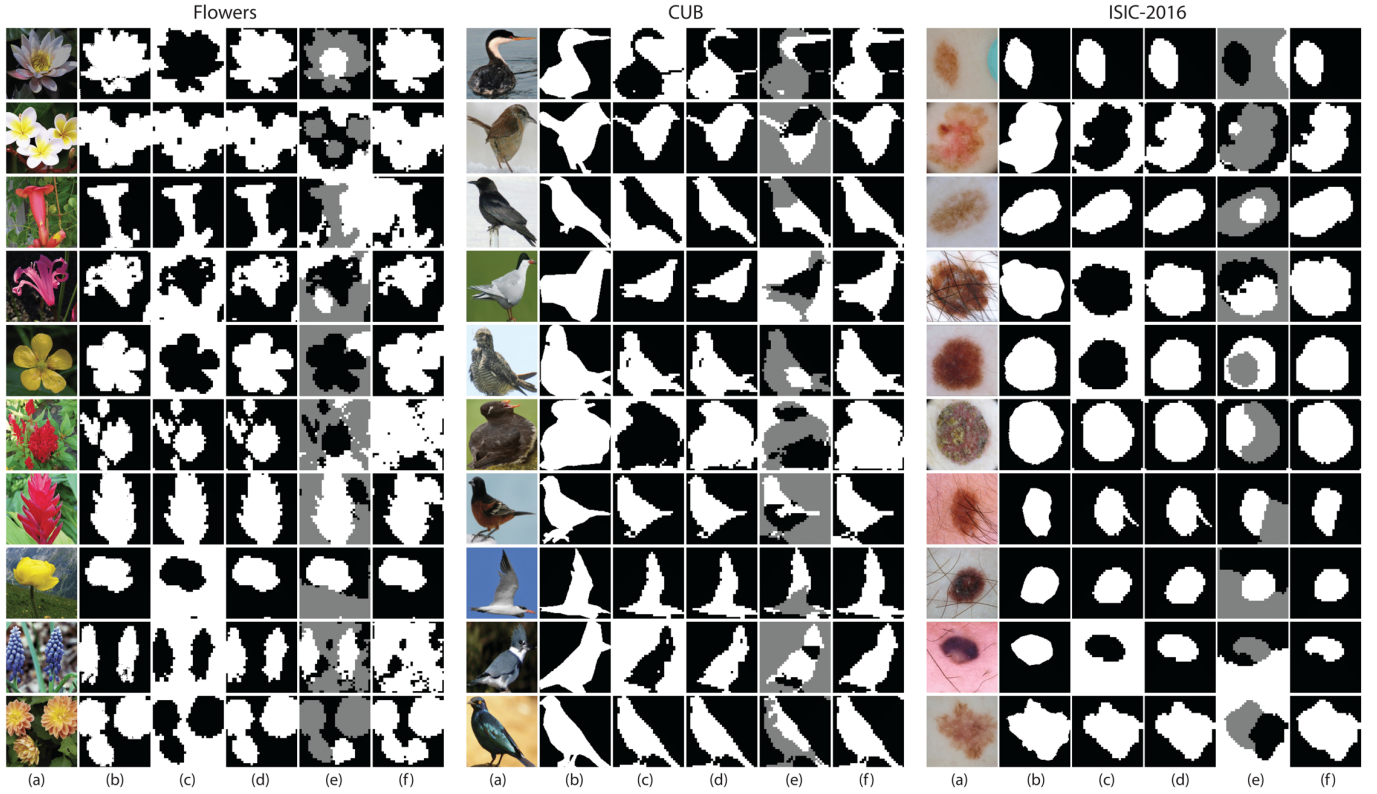


Figure 23: Additional unsupervised image segmentation results on Flowers [37] (*Left Panel*), CUB [51] (*Middle Panel*) and ISIC-2016 [20] (*Right Panel*). (a) input image. (b) ground truth mask. (c) and (e) segmentation results by clustering sparse code vectors per image into 2 or 3 classes using a spectral clustering algorithm. (d) and (f) boundary connectivity information [61] was used to decide the foreground and background.

References

- [1] Peng Bao, Wenjun Xia, Kang Yang, Weiyan Chen, Mi-
anyi Chen, Yan Xi, Shanzhou Niu, Jiliu Zhou, He Zhang,
Huaiqiang Sun, et al. Convolutional sparse coding for com-
pressed sensing ct reconstruction. *IEEE transactions on*
medical imaging, 38(11):2607–2619, 2019.
- [2] Gabriel Barello, Adam S Charles, and Jonathan W Pil-
low. Sparse-coding variational auto-encoders. *BioRxiv*, page
399246, 2018.
- [3] Amir Beck and Marc Teboulle. A fast iterative shrinkage-
thresholding algorithm for linear inverse problems. *SIAM*
journal on imaging sciences, 2(1):183–202, 2009.
- [4] Yoshua Bengio, Aaron Courville, and Pascal Vincent. Rep-
resentation learning: A review and new perspectives. *IEEE*
transactions on pattern analysis and machine intelligence,
35(8):1798–1828, 2013.
- [5] Yoshua Bengio, Nicholas Léonard, and Aaron Courville.
Estimating or propagating gradients through stochastic
neurons for conditional computation. *arXiv preprint*
arXiv:1308.3432, 2013.
- [6] Yaniv Benny and Lior Wolf. Onegan: Simultaneous un-
supervised learning of conditional image generation, fore-
ground segmentation, and fine-grained clustering. In *Com-
puter Vision–ECCV 2020: 16th European Conference, Glas-
gow, UK, August 23–28, 2020, Proceedings, Part XXVI 16*,
pages 514–530. Springer, 2020.
- [7] Adam Bielski and Paolo Favaro. Emergence of object seg-
mentation in perturbed generative models. *Advances in Neu-
ral Information Processing Systems*, 32, 2019.
- [8] Mickaël Chen, Thierry Artières, and Ludovic Denoyer. Un-
supervised object segmentation by redrawing. *Advances in*
neural information processing systems, 32, 2019.
- [9] Ricky TQ Chen, Xuechen Li, Roger B Grosse, and David K
Duvenaud. Isolating sources of disentanglement in varia-
tional autoencoders. *Advances in neural information pro-
cessing systems*, 31, 2018.
- [10] Adam Coates and Andrew Y Ng. The importance of encod-
ing versus training with sparse coding and vector quantiza-
tion. In *Proceedings of the 28th international conference on*
machine learning (ICML-11), pages 921–928, 2011.
- [11] Ingrid Daubechies, Michel Defrise, and Christine De Mol.
An iterative thresholding algorithm for linear inverse prob-
lems with a sparsity constraint. *Communications on*
Pure and Applied Mathematics: A Journal Issued by the
Courant Institute of Mathematical Sciences, 57(11):1413–
1457, 2004.
- [12] Jia Deng, Wei Dong, Richard Socher, Li-Jia Li, Kai Li,
and Li Fei-Fei. Imagenet: A large-scale hierarchical image
database. In *2009 IEEE conference on computer vision and*
pattern recognition, pages 248–255. Ieee, 2009.
- [13] Prafulla Dhariwal, Heewoo Jun, Christine Payne, Jong Wook
Kim, Alec Radford, and Ilya Sutskever. Jukebox: A gener-
ative model for music. *arXiv preprint arXiv:2005.00341*,
2020.
- [14] Rui Ding, Kehua Guo, Xiangyuan Zhu, Zheng Wu, and Li-
wei Wang. Comgan: unsupervised disentanglement and seg-
mentation via image composition. *Advances in neural infor-
mation processing systems*, 35:4638–4651, 2022.
- [15] Patrick Esser, Robin Rombach, and Bjorn Ommer. Taming
transformers for high-resolution image synthesis. In *Pro-
ceedings of the IEEE/CVF conference on computer vision*
and pattern recognition, pages 12873–12883, 2021.
- [16] Kion Fallah and Christopher J Rozell. Variational sparse cod-
ing with learned thresholding. In *International Conference*
on Machine Learning, pages 6034–6058. PMLR, 2022.
- [17] Jacob M Graving and Iain D Couzin. Vae-sne: a deep gen-
erative model for simultaneous dimensionality reduction and
clustering. *BioRxiv*, pages 2020–07, 2020.
- [18] Klaus Greff, Raphaël Lopez Kaufman, Rishabh Kabra, Nick
Watters, Christopher Burgess, Daniel Zoran, Loic Matthey,
Matthew Botvinick, and Alexander Lerchner. Multi-object
representation learning with iterative variational inference.
In *International Conference on Machine Learning*, pages
2424–2433. PMLR, 2019.
- [19] Karol Gregor and Yann LeCun. Learning fast approxima-
tions of sparse coding. In *Proceedings of the 27th inter-
national conference on international conference on machine*
learning, pages 399–406, 2010.
- [20] David Gutman, Noel CF Codella, Emre Celebi, Brian Helba,
Michael Marchetti, Nabin Mishra, and Allan Halpern. Skin
lesion analysis toward melanoma detection: A challenge at
the international symposium on biomedical imaging (isbi)
2016, hosted by the international skin imaging collaboration
(isic). *arXiv preprint arXiv:1605.01397*, 2016.
- [21] Xingzhe He, Bastian Wandt, and Helge Rhodin. Ganseg:
Learning to segment by unsupervised hierarchical image
generation. In *Proceedings of the IEEE/CVF Conference*
on Computer Vision and Pattern Recognition, pages 1225–
1235, 2022.
- [22] Martin Heusel, Hubert Ramsauer, Thomas Unterthiner,
Bernhard Nessler, and Sepp Hochreiter. Gans trained by a
two time-scale update rule converge to a local nash equilib-
rium. *Advances in neural information processing systems*,
30, 2017.
- [23] Irina Higgins, Loic Matthey, Arka Pal, Christopher Burgess,
Xavier Glorot, Matthew Botvinick, Shakir Mohamed, and
Alexander Lerchner. beta-vae: Learning basic visual con-
cepts with a constrained variational framework. In *Interna-
tional conference on learning representations*, 2017.
- [24] Patrik O Hoyer. Non-negative matrix factorization with
sparseness constraints. *Journal of machine learning re-
search*, 5(9), 2004.
- [25] Eric Jang, Shixiang Gu, and Ben Poole. Categorical repa-
rameterization with gumbel-softmax. In *International Con-
ference on Learning Representations*, 2016.
- [26] Justin Johnson, Alexandre Alahi, and Li Fei-Fei. Perceptual
losses for real-time style transfer and super-resolution. In
Computer Vision–ECCV 2016: 14th European Conference,
Proceedings, Part II 14, pages 694–711. Springer, 2016.
- [27] Tero Karras, Samuli Laine, and Timo Aila. A style-based
generator architecture for generative adversarial networks.
In *Proceedings of the IEEE/CVF conference on computer vi-
sion and pattern recognition*, pages 4401–4410, 2019.

- [28] Hyunjik Kim and Andriy Mnih. Disentangling by factorising. In *International Conference on Machine Learning*, pages 2649–2658. PMLR, 2018.
- [29] Diederik P Kingma and Jimmy Ba. Adam: A method for stochastic optimization. *arXiv preprint arXiv:1412.6980*, 2014.
- [30] Diederik P Kingma and Max Welling. Auto-encoding variational bayes. *arXiv preprint arXiv:1312.6114*, 2013.
- [31] Abhishek Kumar and Ben Poole. On implicit regularization in β -vae. In *International Conference on Machine Learning*, pages 5480–5490. PMLR, 2020.
- [32] Abhishek Kumar, Prasanna Sattigeri, and Avinash Balakrishnan. Variational inference of disentangled latent concepts from unlabeled observations. In *International Conference on Learning Representations*.
- [33] Anders Boesen Lindbo Larsen, Søren Kaae Sønderby, Hugo Larochelle, and Ole Winther. Autoencoding beyond pixels using a learned similarity metric. In *International conference on machine learning*, pages 1558–1566. PMLR, 2016.
- [34] Doyup Lee, Chiheon Kim, Saehoon Kim, Minsu Cho, and Wook-Shin Han. Autoregressive image generation using residual quantization. In *Proceedings of the IEEE/CVF Conference on Computer Vision and Pattern Recognition*, pages 11523–11532, 2022.
- [35] Francesco Locatello, Dirk Weissenborn, Thomas Unterthiner, Aravindh Mahendran, Georg Heigold, Jakob Uszkoreit, Alexey Dosovitskiy, and Thomas Kipf. Object-centric learning with slot attention. *Advances in Neural Information Processing Systems*, 33:11525–11538, 2020.
- [36] Maria-Elena Nilsback and Andrew Zisserman. Delving into the whorl of flower segmentation. In *BMVC*, volume 2007, pages 1–10, 2007.
- [37] Maria-Elena Nilsback and Andrew Zisserman. Automated flower classification over a large number of classes. In *2008 Sixth Indian conference on computer vision, graphics & image processing*, pages 722–729. IEEE, 2008.
- [38] Bruno A Olshausen and David J Field. Emergence of simple-cell receptive field properties by learning a sparse code for natural images. *Nature*, 381(6583):607–609, 1996.
- [39] Cheng Ouyang, Konstantinos Kamnitsas, Carlo Biffi, Jinming Duan, and Daniel Rueckert. Data efficient unsupervised domain adaptation for cross-modality image segmentation. In *Medical Image Computing and Computer Assisted Intervention–MICCAI 2019: 22nd International Conference, Shenzhen, China, October 13–17, 2019, Proceedings, Part II* 22, pages 669–677. Springer, 2019.
- [40] Prajit Ramachandran, Barret Zoph, and Quoc V Le. Searching for activation functions. *arXiv preprint arXiv:1710.05941*, 2017.
- [41] Saiprasad Ravishankar, Jong Chul Ye, and Jeffrey A Fessler. Image reconstruction: From sparsity to data-adaptive methods and machine learning. *Proceedings of the IEEE*, 108(1):86–109, 2019.
- [42] Ali Razavi, Aaron van den Oord, Ben Poole, and Oriol Vinyals. Preventing posterior collapse with delta-vae. In *International Conference on Learning Representations*.
- [43] Michal Rolínek, Dominik Zietlow, and Georg Martius. Variational autoencoders pursue pca directions (by accident). In *Proceedings of the IEEE/CVF Conference on Computer Vision and Pattern Recognition*, pages 12406–12415, 2019.
- [44] Carsten Rother, Vladimir Kolmogorov, and Andrew Blake. ” grabcut” interactive foreground extraction using iterated graph cuts. *ACM transactions on graphics (TOG)*, 23(3):309–314, 2004.
- [45] Ron Rubinstein, Alfred M Bruckstein, and Michael Elad. Dictionaries for sparse representation modeling. *Proceedings of the IEEE*, 98(6):1045–1057, 2010.
- [46] Leonid I Rudin, Stanley Osher, and Emad Fatemi. Nonlinear total variation based noise removal algorithms. *Physica D: nonlinear phenomena*, 60(1-4):259–268, 1992.
- [47] Mostafa Sadeghi and Paul Magron. A sparsity-promoting dictionary model for variational autoencoders. *arXiv preprint arXiv:2203.15758*, 2022.
- [48] Pedro Savarese, Sunnie SY Kim, Michael Maire, Greg Shakhnarovich, and David McAllester. Information-theoretic segmentation by inpainting error maximization. In *Proceedings of the IEEE/CVF Conference on Computer Vision and Pattern Recognition*, pages 4029–4039, 2021.
- [49] Francesco Tonolini, Bjørn Sand Jensen, and Roderick Murray-Smith. Variational sparse coding. In *Uncertainty in Artificial Intelligence*, pages 690–700. PMLR, 2020.
- [50] Aaron Van Den Oord, Oriol Vinyals, et al. Neural discrete representation learning. *Advances in neural information processing systems*, 30, 2017.
- [51] C. Wah, S. Branson, P. Welinder, P. Perona, and S. Belongie. The caltech-ucsd birds-200-2011 dataset. Technical Report CNS-TR-2011-001, California Institute of Technology, 2011.
- [52] Yuxin Wu and Kaiming He. Group normalization. In *Proceedings of the European conference on computer vision (ECCV)*, pages 3–19, 2018.
- [53] Xide Xia and Brian Kulis. W-net: A deep model for fully unsupervised image segmentation. *arXiv preprint arXiv:1711.08506*, 2017.
- [54] Jie Xu, Yazhou Ren, Huayi Tang, Xiaorong Pu, Xiaofeng Zhu, Ming Zeng, and Lifang He. Multi-vae: Learning disentangled view-common and view-peculiar visual representations for multi-view clustering. In *Proceedings of the IEEE/CVF International Conference on Computer Vision*, pages 9234–9243, 2021.
- [55] Jianchao Yang, Kai Yu, Yihong Gong, and Thomas Huang. Linear spatial pyramid matching using sparse coding for image classification. In *2009 IEEE Conference on computer vision and pattern recognition*, pages 1794–1801. IEEE, 2009.
- [56] Jiahui Yu, Xin Li, Jing Yu Koh, Han Zhang, Ruoming Pang, James Qin, Alexander Ku, Yuanzhong Xu, Jason Baldridge, and Yonghui Wu. Vector-quantized image modeling with improved vqgan. *arXiv preprint arXiv:2110.04627*, 2021.
- [57] Peiyu Yu, Sirui Xie, Xiaojian Ma, Yixin Zhu, Ying Nian Wu, and Song-Chun Zhu. Unsupervised foreground extraction via deep region competition. *Advances in Neural Information Processing Systems*, 34:14264–14279, 2021.

- [58] Richard Zhang, Phillip Isola, Alexei A Efros, Eli Shechtman, and Oliver Wang. The unreasonable effectiveness of deep features as a perceptual metric. In *Proceedings of the IEEE conference on computer vision and pattern recognition*, pages 586–595, 2018.
- [59] Shengjia Zhao, Jiaming Song, and Stefano Ermon. Infovae: Balancing learning and inference in variational autoencoders. In *Proceedings of the aaai conference on artificial intelligence*, volume 33, pages 5885–5892, 2019.
- [60] Chuanxia Zheng, Long Tung Vuong, Jianfei Cai, and Dinh Phung. Movq: Modulating quantized vectors for high-fidelity image generation. *arXiv preprint arXiv:2209.09002*, 2022.
- [61] Wangjiang Zhu, Shuang Liang, Yichen Wei, and Jian Sun. Saliency optimization from robust background detection. In *Proceedings of the IEEE conference on computer vision and pattern recognition*, pages 2814–2821, 2014.